Detection of vibrating objects in SAR images

6 authors, including:

Balu Santhanam
University of New Mexico
87 PUBLICATIONS   **872** CITATIONS

Armin Walter Doerry
Sandia National Laboratories
214 PUBLICATIONS   **1,266** CITATIONS

Some of the authors of this publication are also working on these related projects:

Project SAR Vibrometry Using Discrete Fractional Fourier Analysis View project

Project Resolution Enhancement for Optical Nanolithography View project

Detection of vibrating objects in SAR images

Francisco Pérez[a], Balu Santhanam[a], Thomas Atwood[a], Ralf Dunkel[b], Armin W. Doerry[c], and Majeed M. Hayat[a,d]

[a]The Center for High Technology Materials and the Electrical and Computer Engineering Department, The University of New Mexico, 1313 Goddard SE Albuquerque, NM, 87106, USA
[b]General Atomics Aeronautical Systems Inc., 14200 Kirkham Way, Poway, CA 92121, USA
[c]Sandia National Laboratories, 1515 Eubank SE Albuquerque, NM 87123, USA
[d]Department of Electrical and Computer Engineering, Marquette University, 1515 W. Wisconsin Ave. Milwaukee, WI 53233, USA

ABSTRACT

The vibratory response of buildings and machines carries key information that can be exploited to infer their operating conditions and to diagnose failures. Moreover, since vibration signatures observed from the exterior surfaces of structures are intrinsically linked to the type of machinery operating inside of them, the ability to monitor vibrations remotely can facilitate the detection and identification of the machinery. Recently, synthetic aperture radar (SAR) has proven to be a versatile tool capable of performing vibrometry and high-precision vibration-estimation algorithms have been developed for reconstructing surface vibration waveforms from SAR images. However, these algorithms tend to be computationally demanding and, in addition, require knowledge of the exact location of the object a priori. This renders their use as unpractical for exploratory applications. This paper focuses on the detection of vibrating objects by exploiting the phase modulation that a vibration causes in the received slow-time SAR data. Two different vibration detection schemes are investigated. The first scheme is data-driven and utilizes features extracted with the help of the discrete fractional Fourier transform (DFrFT) to feed a random-forest detector. The second scheme is model-based, and uses a probabilistic model of the slow-time SAR signal, the Karhunen-Loève expansion, and a likelihood-ratio detector. The proposed detection algorithms are tested using both simulated and real SAR data. Our results show that both detection schemes can be used to achieve high-performance vibrating-object detectors.

Keywords: Synthetic aperture radar, vibration detection, discrete fractional Fourier transform, time-frequency analysis, Karhunen-Loève expansion, machine-learning algorithms

1. INTRODUCTION

The vibratory response of buildings and machines carries key information that can be exploited to infer their operating conditions and to diagnose failures. Furthermore, since vibration signatures observed from the exterior surfaces of structures are intrinsically linked to the type of machinery operating inside of them, the ability to monitor vibrations remotely can facilitate the detection and identification of the machinery. Recently, synthetic aperture radar (SAR) has proven to be a versatile tool capable of performing vibrometry[1,2] and many high-precision vibration-estimation algorithms have been developed for reconstructing surface-vibration waveforms from SAR images.[1–5] However, these algorithms tend to be computationally demanding and, in addition, require knowledge of the exact location of the object a priori. This renders their use as unpractical for exploratory applications. The next challenge towards a complete characterization and understanding of surface vibrations in SAR images is in the development of algorithms for detecting and classifying vibrating objects based on their SAR signature.

Further author information: (Send correspondence to Francisco Pérez, Balu Santhanam or Majeed M. Hayat)
Francisco Pérez: E-mail: franperez@unm.edu
Balu Santhanam: E-mail: bsanthan@unm.edu, Telephone: +1 (505) 277-2436
Majeed M. Hayat: E-mail: majeed.hayat@marquette.edu, Telephone: +1 (414) 288-7772

An underlying assumption when forming a SAR image is that all the targets on the ground scene are static. Any vibrational movement of targets in the range direction in the ground scene engenders a Doppler shift, namely a micro-Doppler shift in the returned SAR signal.[6] This micro-Doppler shift causes the vibrating target to present a smearing effect in SAR images. This smearing manifests itself as ghost images surrounding the vibrating target at the same range line and obscuring the actual target shape.[1,2] Figure 1 (b) illustrates the difference between a static target and a vibrating target on a real SAR image generated with the Lynx SAR. While these ghost artifacts degrade the image quality for visual target identification, they do create vibration signatures that can be exploited for retrieving key information. By taking advantage of these signatures, it is shown that we can perform identification, retrieve machinery status, and thus detect prohibited activities. In general, these vibration signatures may include transient signals like chirped sinusoids, and their associated base frequencies and chirp rates.
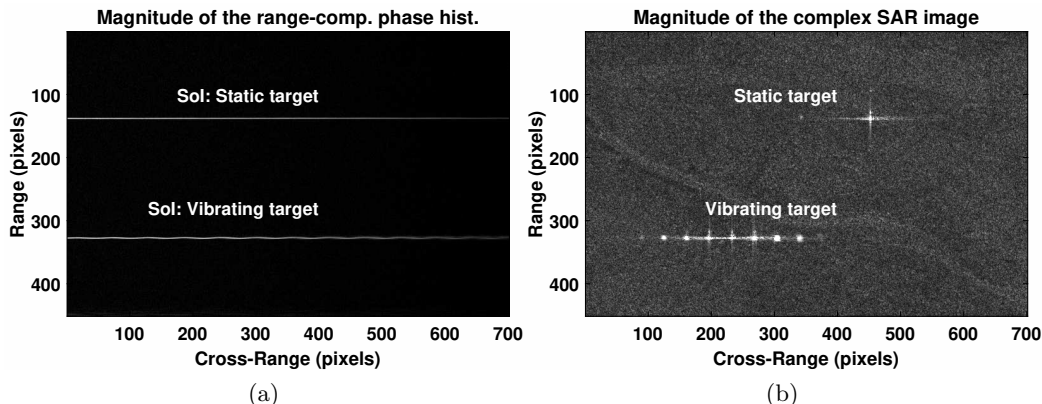

Figure 1: Reconstruction of a SAR image from its range-compressed phase history. (a) The magnitude of the range-compressed SAR phase history containing one static target and one vibrating target. The two targets are separated in range after range compression. (b) The reconstructed SAR image using the SAR phase history in (a). The vibrations of the target introduces ghost artifacts along the azimuth (cross-range) direction. The targets used in this experiment are quad-corner reflectors

In the past, a method based on a cyclostationary model and the generalized likelihood ratio was proposed to detect vibrating objects from slow-time SAR signals.[7] This detection scheme was based on the correlation between the cyclic spectral density (CSD) of a slow-time signal and a stored template of the expected CSD of the vibration. However, as it is shown in Fig. 2, the match between a vibration CSD template and the CSD of the input signal is susceptible to errors because the CSD of SAR signals is impulsive in nature, it is affected by signal noise and terrain clutter, and it also changes with the vibration frequency. Furthermore, this detection scheme is unpractical for more complex types of vibrations, such as chirped vibrations, for which the CSD does not produce a reliable characterization.

This paper focuses on developing novel detection schemes for vibrating objects in SAR images. Two schemes for the detection of vibrating objects from SAR signatures are developed. The first detection scheme is a model-based data-driven approach that utilizes features extracted with the help of the discrete fractional Fourier transform (DFRFT)[8] to feed a machine-learning classifier. Model-based data-driven approaches are appealing because they use data generated via simulation to train machine learning algorithms, supplying in this way the need of thousands of samples that the training of these type classifiers normally require. For this purpose, SAR data is simulated combining the signal model for the SAR slow-time history and different vibration waveforms. Specifically, in this approach the DFRFT is applied to a reconstructed instantaneous frequency (IF) of the slow-time SAR data. The second detection scheme is purely model-based and uses a probabilistic model of the SAR slow-time signal, the Karhunen-Loève transform (KLT),[9] and a likelihood-ratio detector. The results after testing the two detection schemes with both simulated and real SAR data show that both detection schemes can be used to achieve high-performance vibrating-object detectors.
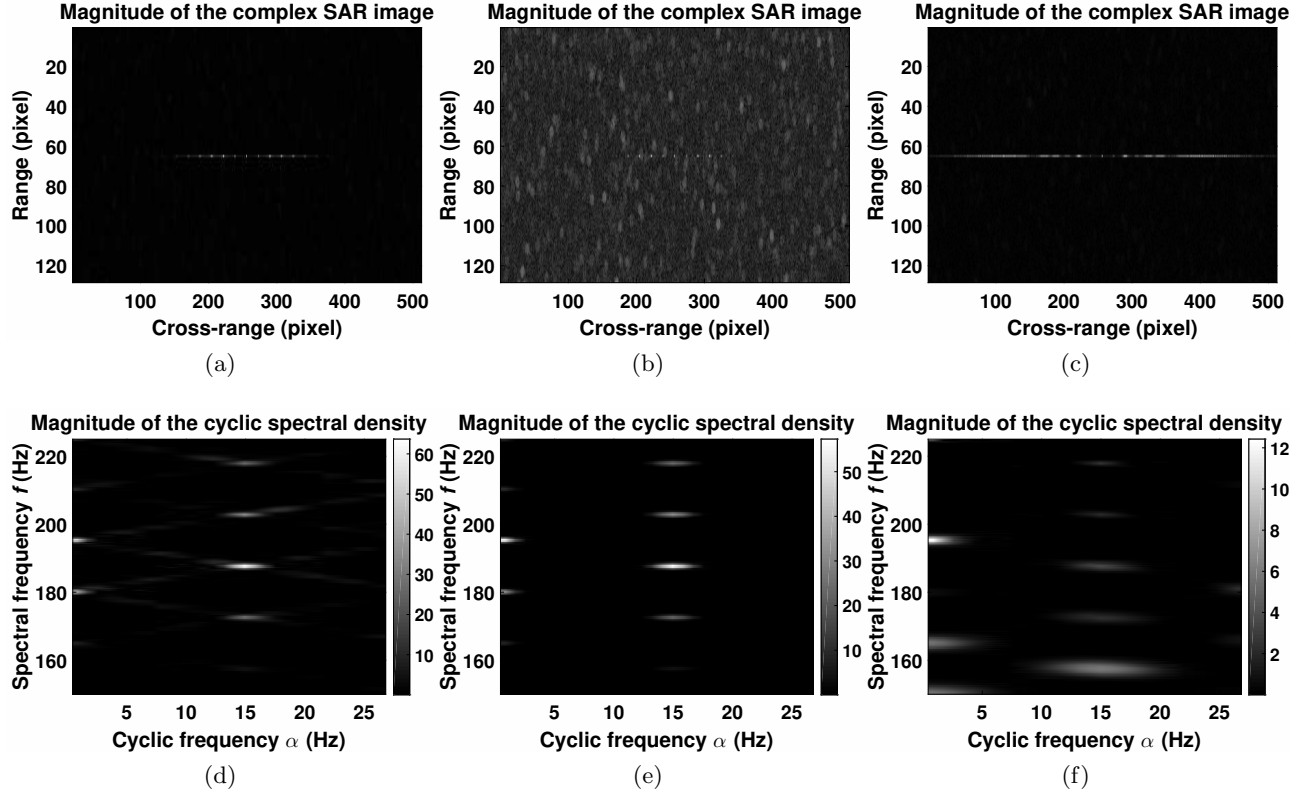
Figure 2: Analysis of vibrating objects in SAR images using the CSD. (a) SAR image containing a vibrating point-object exhibiting a 1.5mm, 15Hz simple sinusoidal vibration. (b) SAR image containing the same object as in (a) with additive clutter and noise at SCR=10dB and SNR=10dB. (c) SAR image containing the same object as in (a) exhibiting also a chirp acceleration at 1Hz/s. (d), (e), (f) are the CSD planes of the corresponding slow-time signals at range 65 of (a), (b) and (c), respectively. The SAR images were generated via simulation using the signal model described in Sec. 2.

2. SIGNAL MODEL

The small range perturbation of the vibrating target modulates the collected SAR phase history. Consider a spotlight-mode SAR whose transmitted pulse is a chirp signal, with carrier frequency and the chirp rate f_c and K, respectively. Each returned SAR pulse is demodulated by the transmitted pulse delayed appropriately by the round-trip time to the center of the illuminated patch. A demodulated pulse can be written as [10, Ch. 1]

$$r(t) = \sum_i \sigma_i \exp\left[-j\frac{4\pi(r_i - r_c)}{c}\left(f_c + K(t - \frac{2r_c}{c})\right)\right], \tag{1}$$

where σ_i is the reflectivity of the ith scatterer, c is the propagation speed of the pulse, and r_c is the distance from the patch center to the antenna. The polar-to-rectangular resampling approach is then applied to the SAR phase history [10, Sec. 3.5] to correct for range cell migration. Autofocus is also performed at this stage. For small vibrations, the vibration-induced phase modulation in range direction is very small;[11–13] therefore, it is ignored. Range compression is applied to the phase history to separate the scatterers in range. Figure 1 shows the magnitude of the range-compressed SAR phase history containing one static point target and one vibrating point target. Assuming that all scatterers at a specific range are static, the range-compressed phase history at this specific range can be written as

$$s[n] = \sum_i \sigma_i[n]\exp\left[j\left(f_y y_i n - \frac{4\pi f_c}{c}r_i + \phi_i\right)\right] + w[n], \tag{2}$$

for $0 \le n < N-1$, where n is the index of the collected returned pulses, N represents the total number of collected returned pulses, y_i is the cross-range position of the ith target, and ϕ_i represents all additional (constant) phase terms. The imaging factor, f_y, is known and used to estimate the cross-range of the target. For spotlight-mode SAR, f_y can be written as[10, 14]

$$f_y = \frac{4\pi f_c}{c} \frac{V}{R_0 f_{prf}}, \tag{3}$$

where V is the nominal speed of the SAR antenna, R_0 is the distance from the patch center to the mid-aperture, and f_{prf} is the pulse-repetition frequency (PRF). The SAR integration time is given by $T_I = f_{prf}N$, and $w[n]$ is additive noise.
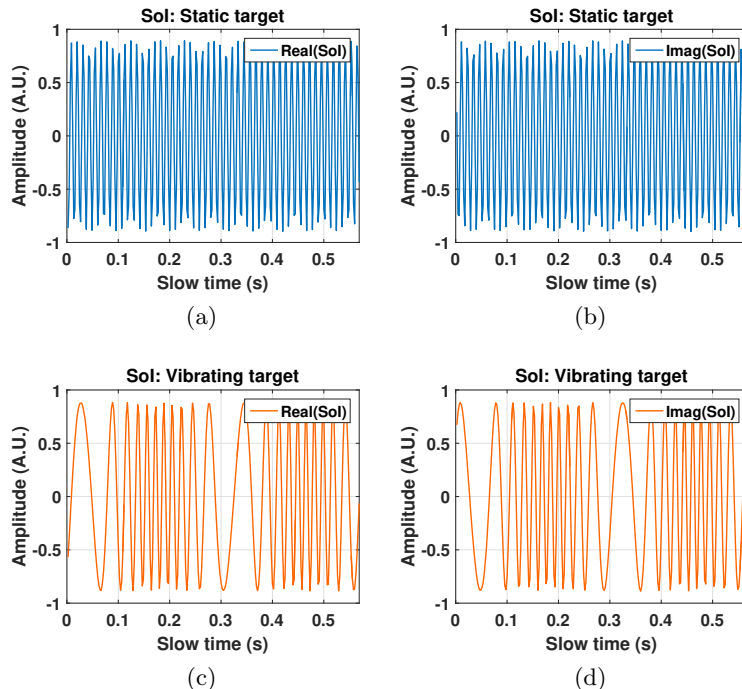

Figure 3: Example of the slow-time signal for a static and a vibrating targets. Complex SoI simulated for a (a,b) static target, (c,d) vibrating target. In (c,d) the target vibration induces phase modulation on the signal of (a,b). The vibration was a sinusoidal function of amplitude 1cm and frequency 3.5Hz. The Lynx radar parameters of Table 1 and the signal model (4) were used for generating the signals.

The signal $s[n]$ in (2) is a stationary signal if all scatterers are static. The azimuth compression, accomplished by applying the discrete Fourier transform (DFT) to $s[n]$, will focus the static scatterers on the correct cross-range positions. However, when a vibrating scatterer is present, $s[n]$ has a non-stationary component because r_i is now a function of n for the vibrating scatterer. The cross-range y_i is also changing for the vibrating scatterer. However, because R_0 is very large (tens of kilometers), f_y is usually much smaller than $4\pi f_c/c$; therefore, the phase modulation induced by time-varying y_i is ignored.[12, 13] As such, $\bar{y}_i$ is used to denote the average cross-range position of the vibrating scatterer. For the same reason, a small change in r_i causes a relatively large fluctuation in the Doppler frequency $f_y y_i$. It is important to emphasize that azimuth compression cannot focus the vibrating scatterer on the correct cross-range position because the DFT spectrum of the non-stationary component usually has significant side lobes.[6] Figure 1 (b) shows the reconstructed SAR image by applying azimuth compression to the phase history as shown in Fig. 1 (a). The side lobes near the vibration target are commonly referred to as the *ghost targets*.[6] The vibration-induced phase modulation is referred to as the *micro-Doppler effect*.[13] Analysis tools other than the DFT are required to estimate and characterize vibrations and non-stationary targets in general.

The signal of interest (SoI) is defined as the slow-time signal (range line) in the range-compressed phase

history containing vibrating targets. Figure 1 (a) shows the magnitude of the SoI of both a static target and a vibrating target, displayed in a range-compressed phase history image. Figure 3 shows the SoI of a static target and a vibrating target displayed as functions of the slow time.

When a vibrating scatterer is well-separated from other scatterers in range, which may be possible by choosing a proper data collection orientation, the SoI can be written as

$$s[n] = \sigma[n] \exp\left[j\left(f_y \bar{y} n - \frac{4\pi f_c}{c} r_d[n] + \phi\right)\right] + w[n] \tag{4}$$

for $0 \leq n < N - 1$.

All the simulations of SAR signals performed in this paper make use of 4 in conjunction with the Lynx radar parameters of Table 1.

Table 1: SAR system parameters for simulations. The paremeters were extracted from SAR images generated with the Lynx radar oeprating at 1ft. resolution.

Parameter	Quantity
Pixel dimension	$0.25 \times 0.25\text{m}^2$
Nominal resolution	$0.3 \times 0.3\text{m}^2$
Carrier frequency	$f_c = 16\text{GHz}$
Slant range	$R_0 = 10\text{Km}$
Plane velocity	$V = 100\text{m/s}$
Effective pulse-repetition frequency	$f_{prf} = 450\text{Hz}$
Number of collected pulses	$N = 1024$
SNR	30dB
SCR	30dB

3. VIBRATION DETECTION: BINARY HYPOTHESIS TESTING PROBLEM

In the signal model for the SAR SOI (4), the term $r_d[n]$ is the projection of the instantaneous position of the target onto the line of sight from the target to the SAR. Hence, when the target is static, the term $r_d[n]$ is a constant for all slow-time index n, but when the target is vibrating, $r_d[n]$ is the projection of the vibration displacement and, therefore, it varies over time. The only exception to this is when the vibration is unidirectional and it occurs parallel to the flight path of the sensor. This will cause the slow-time signal of the vibrating object to be identically as the slow-time signal of a static object. Nevertheless, this will not be considered as a concern because when imaging a site using an airborne SAR system, multiple passes from different azimuthal angles can be performed in order to ensure capturing micro-Doppler modulation of vibrating objects. Therefore, in consideration of the signal model (4) a binary hypothesis-testing problem is defined as follows. The null hypothesis, H_0, represents the case in which the slow-time signal, $s[n]$, contains the return $s_0[n]$ from a static object; and the alternative hypothesis, H_1, represents the case in which the slow-time signal, $s[n]$, contains the return $s_1[n]$ from a vibrating object. In this formulation, it will be assumed that $r_d[n]$ is a pure sinusoidal function. Also, without loss of generality, the constant phase terms in the signal model can be combined into a single one. Then, the hypotheses for a point object in a SAR image can be stated as follows:

$$\begin{aligned} H_0 &: s[n] = s_0[n] + w[n] = \sigma \exp\left(j f_y \bar{y} n + j\phi\right) + w[n], \\ H_1 &: s[n] = s_1[n] + w[n] = \sigma \exp\left(j f_y \bar{y} n + j\phi + j x[n]\right) + w[n], \end{aligned} \tag{5}$$

where $x[n] = \frac{4\pi f_c}{c} r_d[n]$ and it is been assumed that the reflectivity of the target σ does not change for $0 \leq n < N - 1$. Since in a SAR image the slow-time signal at a given range position consists of a total of N samples, the

hypothesis-testing problem can be restated in the following vector form

$$H_0 : \mathbf{s} = \begin{bmatrix} s[0], \ldots, s[N-1] \end{bmatrix}^T = \mathbf{s}_0 + \mathbf{w} = \begin{bmatrix} s_0[0] \\ \vdots \\ s_0[N-1] \end{bmatrix} + \begin{bmatrix} w[0] \\ \vdots \\ w[N-1] \end{bmatrix},$$

vs.

$$H_1 : \mathbf{s} = \begin{bmatrix} s[0], \ldots, s[N-1] \end{bmatrix}^T = \mathbf{s}_1 + \mathbf{w} = \begin{bmatrix} s_1[0] \\ \vdots \\ s_1[N-1] \end{bmatrix} + \begin{bmatrix} w[0] \\ \vdots \\ w[N-1] \end{bmatrix}.$$

(6)

Therefore, given a slow-time vector $\mathbf{s} = \begin{bmatrix} s[0], \ldots, s[N-1] \end{bmatrix}^T$ from a SAR image, the ultimate goal is to determine if $\mathbf{s}$ belongs either to H_0 or H_1.

4. VIBRATION DETECTION SCHEME BASED ON A RANDOM FOREST AND THE DFRFT

This detection scheme is a model-based data-driven approach for classifying vibration signatures in SAR images. Model-based data-driven approaches are appealing because they use data generated via simulation to train machine learning algorithms, supplying in this way the need of thousands of samples that the training of these type classifiers normally require. For this purpose, SAR data is simulated combining the signal model for the SAR slow-time history (4) and different vibration waveforms.

The feature extraction process make use of the smoothed pseudo Wigner–Ville time-frequency distribution (SPWVTFD) and the DFRFT. First, in order to reconstruct the IF of the slow-time signal, the SPWVTFD is applied to the vector $\mathbf{s} = \begin{bmatrix} s[0], \ldots, s[N-1] \end{bmatrix}^T$ consisting of N samples of the slow-time signal at given range coordinate of the SAR image. The SPWVTFD is a bilinear time-frequency transform designed to reduce the cross-term interference of the Wigner-Ville time-frequency distribution.[13, 15] Similarly to a Fourier spectrogram, the SPWVTFD does not yield a direct, quantitative interpretation of IF of the signal but instead it produces a graphical illustration of it, which must be further interpreted and analyzed if multiple frequencies or non-stationary frequencies are present in the vibration. A more detailed description of the SPWVTFD is given in.[13, 15] Nevertheless, here it is assumed that the instantaneous position of vibration can be recovered from the SPWVTFD of the SAR slow-time signal by comparing its magnitude with a threshold. Once an estimation of the vibration waveform is obtained, then the DFRFT is applied to characterize the vibration in terms of number of components, center-frequency and chirp-rate of each component. The DFRFT, or more specifically the multi-angle centered-discrete fractional Fourier transform (MA-CDFRFT)[8] is a parametric extension of the centered-DFT that describes the magnitude and phase of signals consisting in sinusoids of given frequency and chirp-rate. A more detailed description of the MA-CDFRFT is given in.[16–18] Even though the traditional DFT is sufficient for characterizing simple sinusoidal vibrations, the use of the DFRFT has the advantage that this same approach can be used for more complex type of vibration, such as chirped vibrations, without the need of changing the feature extraction process. Finally, the feature extraction process concludes by also computing the kurtosis, variance, energy and histogram of the vibration waveform recovered via SPWVTFD. Algorithm 1 summarizes the feature extraction process of this detection scheme and Fig. 4 illustrates the feature extraction process step by step.

The selected machine-learning architecture is a random-forest classifier (RFC).[19] This RFC averages the predictions of multiple decision trees on random subsets of the feature space and it produces a non-linear division of the feature space. The RFC is trained using a 3-fold procedure with stratification and no further hyperparameter tuning. Specifically, this RFC corresponds to the implementation available in the Tensorflow library for Python.[20]
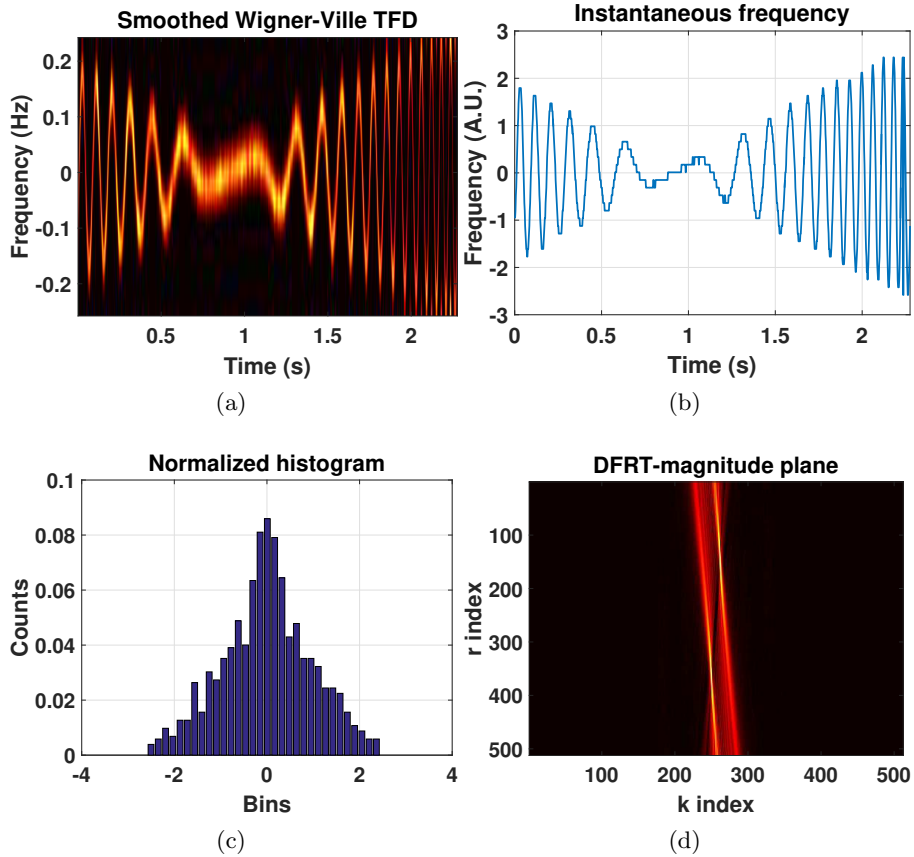
Figure 4: Feature extraction using the SPWVTFD and the DFRFT. (a) SPWVTFD of a SAR signal generated from a object exhibiting a chirp vibration. (b) IF recovered from (a) by thresholding. (c) Normalized histogram of (b) using 32 bins. (d) Magnitude plane of the 512-points DFRFT of (b).

Algorithm 1 Feature extraction using the SPWVTFD and the DFRFT.

1: $\mathbf{s} = \big[s[0], \ldots, s[N-1]\big]^T$: a slow-time vector from a SAR image.
2: Apply the SPWVTFD to $\mathbf{s}$ to generate a N_b-frequency-bins spectrogram of the slow-time signal (e.g. N_b=32).

3: The IF curve (vibration waveform) of the slow-time signal is then extracted from the previous spectrogram using thresholding.
4: Compute the kurtosis and variance and energy on the extracted IF curve.
5: Compute the N_b-bins histogram of the IF.
6: Apply the DFRFT to the IF and store the information of the N_c-most prominent peaks of magnitude plane (e.g. N_c=6). Specifically, the magnitude of each peak, its center frequency and its chirp-rate value are considered.
7: Finally, the features computed in 4), 5) and 6) are concatenated in a single feature vector of dimension $N = N_b + 3 + 3N_c$ (e.g. 53×1, for N_b=32 and N_c=6).

---

5. VIBRATION DETECTION SCHEME BASED ON PROBABILISTIC MODEL OF THE SAR SLOW-TIME SIGNAL AND THE KLT

5.1 Probabilistic model for the SAR slow-time signal

Recall the hypothesis testing problem (5) and (6) for an N-samples slow-time vector, where $s_0[n]$ is the part of the slow-time signal that corresponds to the return of a static object, $s_1[n]$ is the part of the slow-time signal

that corresponds to the return of a vibrating object, and $w[n]$ is an additive term to represent noise and clutter. Due to physical properties of a SAR, there are natural constraints for the variables σ, ϕ, $\bar{y}$ for an object within a SAR image. Similarly, due the limitations of a SAR a vibration sensor,[1] some constraints also applies to the vibration waveform (instantaneous position) $x[n]$, $0 \leq n \leq N-1$. In light of this limitations, consider the following probabilistic model of (5) for a vibration described by a simple sinusoidal function

$$
\begin{aligned}
H_0 &: S[n] = S_0[n] + W[n] = \Sigma \exp\left(jf_y Yn + j\Phi\right) + W[n], \\
H_1 &: S[n] = S_1[n] + W[n] = \Sigma \exp\left(jf_y Yn + j\Phi + jX[n]\right) + W[n],
\end{aligned} \tag{7}
$$

where $\Sigma \sim U[\sigma_{min}, \sigma_{max}]$ (the symbol "$\sim$" means "distributed as") is the reflectivity of the object, $Y \sim U[-y_o, y_o]$ is its cross-range coordinate (deviation from the center of the SAR image) with $y_o > 0$, $\Phi \sim U[-\pi, \pi]$ is a constant (yet random) phase term, and $W[n] \sim \mathcal{CN}(0, \sigma_w^2)$ is circularly-symmetric complex Gaussian noise, $0 \leq n \leq N-1$. The term $X[n] = A\cos(\Phi_x + 2\pi nF)$ is the projection of the instantaneous position of the vibrating object onto the line of sight from the object to the SAR, where $\Phi_x \sim U[-\pi, \pi]$ is a vibration phase term, $F \sim U[f_{min}, f_{max}]$ is directly proportional to the vibration frequency, and $A \sim U[a_{min}, a_{max}]$ is directly proportional to the vibration amplitude. The scaling factor for the vibration frequency is $1/f_{prf}$, and for the vibration amplitude is $\frac{4\pi f_c}{c}$. It is important to recall that all the parameters that determine the distribution of these random variables can be estimated from the SAR specifications. In the vector form of the hypothesis testing problem (6), the random variables $S[0], S[1], \ldots, S[N-1]$ are correlated under both hypotheses. However, the noise samples $W[0], W[1], \ldots, W[N-1]$ are considered to be independent and identically distributed.

5.2 Karhunen-Loève expansion

The Karhunen-Loève (KL) expansion allows one to decorrelate the components of the slow-time vector $\mathbf{S}$, therefore, it allows one to work with simpler probability density functions. Specifically, in the KL expansion the eigenvectors of the covariance matrix of the signal capture the temporal correlation of the signal. The randomness of $\mathbf{S}$ is captured in the KL coefficients which correspond to the projections of $\mathbf{S}$ onto the set of eigenvectors of the covariance matrix.

Recall the hypothesis testing problem defined in the previous section (7), where the reflectivity, phase and position of a point object are modeled as random variables as well as the amplitude, frequency and phase of the simple sinusoidal vibration $X[n] = A\cos(\Phi_x + 2\pi nF)$. In order to construct a detection scheme based on the KLT the first step is to compute the covariance matrices of the slow-time vector $\mathbf{S}$ under both hypothesis, H_0 and H_1. This is performed in App. A. Once the covariance matrices are determined, the next step is to obtain the KL coefficients from the slow-time vector $\mathbf{S}$ using the KL expansion as described in App. B

5.3 Likelihood ratio detector based on the Karhunen-Loève expansion

Based on the previous KL expansion it is possible to define a new likelihood ratio as a decision tool for detecting vibrating objects in SAR images. For this purpose, given a signal $\mathbf{S}$ from a SAR image, a likelihood ratio function of using its KL coefficients is defined.

A slow-time signal $\mathbf{s} = \left[s[0], \ldots, s[N-1]\right]^T$ can be expanded using the eigenvectors of the covariance matrix computed under each hypothesis. This is, given a slow-time vector $\mathbf{s}$ from a SAR image, one can compute the KL coefficients under H_0, $z_k^0 = (\mathbf{v}_k^0)^* \mathbf{s}$, and under H_1, $z_k^1 = (\mathbf{v}_k^1)^* \mathbf{s}$, for $k = 0, 1, 2, \ldots, N-1$. If $\mathbf{S}$ is assumed to be complex-normal distributed, then resulting KL coefficients are also complex-normal distributed (and zero-mean, because $\mathbf{S}$ is zero-mean) since they are a linear combination of complex-normal distributed random variables (38). Therefore, they can be completely described by their first- and second-order statistics. Furthermore, since the KL coefficients are independent, we have

$$
Z_k^0 \sim \mathcal{CN}(0, \lambda_k^0), \quad \text{and} \quad Z_k^1 \sim \mathcal{CN}(0, \lambda_k^1), \tag{8}
$$

where λ_k^0 and λ_k^1 are the eigenvalues of $\mathbf{cov}\{\mathbf{S}\}$ under H_0 and H_1, respectively. Therefore, in this case the equivalent hypothesis testing problem can be stated as

$$
\begin{aligned}
H_1 &: \mathbf{Z} = \{Z_k\}_{k=0}^{N-1}, \quad Z_k\text{'s independent, with } Z_k \sim \mathcal{CN}(0, \lambda_k^1) \\
H_0 &: \mathbf{Z} = \{Z_k\}_{k=0}^{N-1}, \quad Z_k\text{'s independent, with } Z_k \sim \mathcal{CN}(0, \lambda_k^0).
\end{aligned} \tag{9}
$$

Algorithm 2 Vibration detection scheme using a probabilistic model and the KL expansion.

1: Determine the distributions of $\Sigma, Y, \Phi, A, f, \Phi_x$ based on radar specifications.
2: Compute the covariance matrices under hypothesis H_0 and H_1 using (26) and (35), respectively.
3: Perform the spectral decomposition of the two covariance matrices (36).
4: For every slow-time vector $\mathbf{s} = \left[s[0], \ldots, s[N-1] \right]^T$, compute $\{z_k^0\}_{k=0}^{N-1}$ and $\{z_k^1\}_{k=0}^{N-1}$ using (38) and the eigenvectors of $\mathbf{cov}(\mathbf{S})$ under H_0 and H_1, respectively.
5: Compute the likelihood ratio (11).
6: Compare the likelihood ratio with a threshold to determine if $\mathbf{s}$ belongs either to H_0 or H_1.

Then, it is possible to define a likelihood ratio for a slow-time vector $\mathbf{s}$ consisting of N samples, i.e., consisting of N KL coefficients under each hypothesis, as

$$L(\mathbf{s}) = \frac{f_{\mathbf{S}}(\mathbf{s})\big|_{H_1}}{f_{\mathbf{S}}(\mathbf{s})\big|_{H_0}} = \frac{f_{\mathbf{Z}}(\mathbf{z})\big|_{H_1}}{f_{\mathbf{Z}}(\mathbf{z})\big|_{H_0}} = \frac{\prod_{k=0}^{N-1} \frac{1}{\pi\lambda_k^1} \exp\left(-\frac{|z_k^1|^2}{\lambda_k^1} \right)}{\prod_{k=0}^{N-1} \frac{1}{\pi\lambda_k^0} \exp\left(-\frac{|z_k^0|^2}{\lambda_k^0} \right)}, \tag{10}$$

$$L(\mathbf{s}) = \prod_{k=0}^{N-1} \frac{\lambda_k^0}{\lambda_k^1} \exp\left(\frac{|z_k^0|^2}{\lambda_k^0} - \frac{|z_k^1|^2}{\lambda_k^1} \right). \tag{11}$$

The latter expression defines a likelihood ratio that can be compared with a threshold in order to decide if the slow-time signal $\mathbf{s}$, via its KL coefficients $\{z_k^0\}_{k=0}^{N-1}$ and $\{z_k^1\}_{k=0}^{N-1}$, corresponds to a signal generated by a vibrating object or a static object. Algorithm 2 summarizes the steps involved in this detection scheme.

6. PERFORMANCE EVALUATION OF THE PROPOSED DETECTORS

The performance of the proposed algorithms is tested using both simulated and real SAR data. The purpose of this study is to understand the limits of the proposed detection schemes, characterize their performance in terms of the receiver operating characteristic (ROC) curve, and study their robustness against a mixed dataset of real SAR data, which contains data from a collection of different vibrometry experiments.

6.1 Dataset description

Two datasets are used to study the performance of the binary detectors. A simulated dataset, consisting of SAR images generated via simulation using the parameters of the Lynx Radar, see Table 1, is used to test the proposed detectors. Specifically, 80% of the dataset is used for training and validation of the RFC. The remaining 20% is used to evaluate the performance of the all the proposed detectors. A second dataset, consisting of real SAR images collected with the Lynx Radar is also used to report the performance of the proposed detectors. The purpose of these two datasets is, one, to study how feasible is to develop data-driven model-based detectors for the vibrating objects in SAR images and two, to test the performance of the proposed detectors using real SAR data. The details of each one of these two dataset is provided below.

Simulated dataset:
The vibrating objects were simulated using single-component sinusoidal vibrations with amplitude between 8mm and 1.5cm, and frequency between 2Hz and 10Hz. For the two classes of objects, the simulated data was contaminated with additive noise and additive clutter at a signal-to-noise ratio (SNR) of 30dB and a signal-to-clutter ratio (SCR) of 30dB. The noise was simulated as independent circularly symmetric complex Gaussian distributed samples. The clutter magnitude was generated by performing circular averaging filter on uniformly random distributed clutter matrix of the same dimensions of the radar synthetic aperture. The circular averaging filter employed a kernel of size of 3×3 pixels. The clutter phase was considered to be uniformly distributed between $-\pi$ and π. A total of 5,000 samples per class were generated. The division of samples within the dataset was 50% and 50% between static objects and vibrating objects. The objects were simulated assuming a deviation no

greater than 15% from the center of the SAR image.

Lynx dataset:
This dataset contains a total of 200 samples of SAR slow-time signals collected in previous vibrometry experiments. One hundred of this samples correspond to static objects and the remaining 100 samples correspond to vibrating objects. This dataset is heterogeneous in terms of resolution and contains SAR signatures collected at resolutions of 1-foot and 4-inches. Also, the plane velocity parameter varies from 80m/s to 100m/s and the effective-pulse-repetition frequency between 200Hz-500Hz. The SNR of the samples of this dataset is roughly 30dB. Similarly, the SCR of the samples of this dataset is also 30dB. The carrier frequency and R0, the distance to the center of the patch, are as in Table 1. Quad-corner reflectors were used as study objects (point-objects). The vibrations were induced by off-balanced motors and had frequency in the range 2Hz-6Hz and amplitude between 2mm and 5cm. The position of the objects had a deviation less than 15% from the center of the SAR image.

6.2 Performance metrics

The performance of the proposed vibration-detection algorithms is mainly measured using the ROC curve and its convexity as indicators. Specifically, the ROC curve reports how well a detector performs in terms of detection ratio vs false-alarm ratio. The ROC curve, in the case of the RFC, is computed by recording the performance while moving boundaries in the feature space and, in the case of the likelihoodratio-based probabilistic detectors, by increasing and decreasing the threshold. The convexity of the ROC curve is quantified by the area under the ROC curve (AUROCC). In addition, the feature usage in the construction of the random forest classifier is also analyzed for studying the suitability of the feature extraction process proposed in Sec. 4.

6.3 Performance evaluation

The performance evaluation of the proposed detectors is presented in Fig. 5 and Table 2. As can be observed, the performance of the RFC is slightly higher than the performance of the probabilistic detector on the simulated dataset. The reason behind this is likely to be a slight overfitting of the data. On the Lynx dataset the performance of both detectors drops about 0.076 to 0.191 in terms of the AUROCC and the probabilistic detector is the one that achieves the highest performance with a AUROCC of 0.899. This indicates that among the two detection algorithms, the probabilistic detectors tend to be more robust against modeling errors in the data. This observation is consistent with the fact that the noise was modeled in the formulation of the probabilistic detectors while the other approach only counts with the time-frequency smoothing of the SPWVTFD. For example, on the Lynx dataset for a false-alarm ratio of 10%, the RFC achieves a true positive rate of 50% and the probabilistic detector 75%. The mismatches in performance reported in the two datasets may be attributed to several modeling errors including but not limited to: (i) Not perfect radar cross-section modeling, since the objects contained in the Lynx dataset are quad-corner reflectors and not ideal point-objects; (ii) variations of radar parameters across the Lynx dataset, since the Lynx dataset contains data from different vibrometry experiments collected at different PRF and resolution.

Table 2: Area under the ROC curve of the proposed detectors for the binary detection problem.

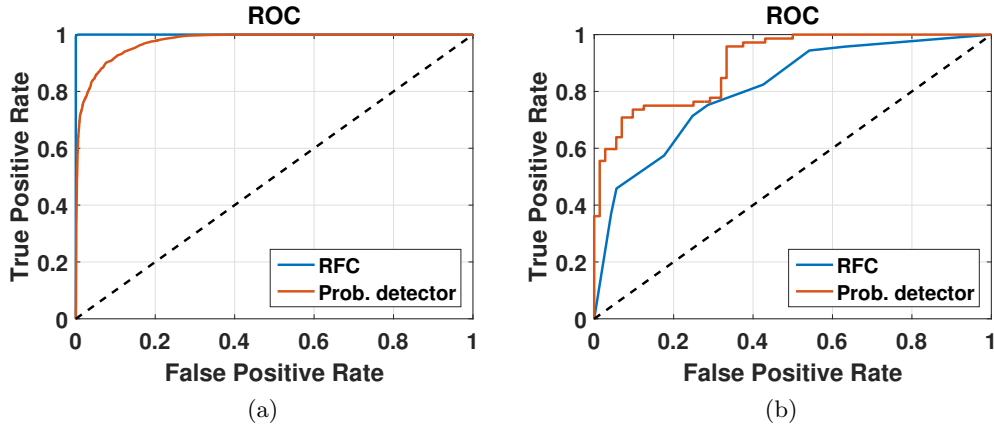| Classifier	Simulated dataset	Lynx dataset
RFC	0.999	0.808
Prob. detector	0.975	0.899

Figure 5: ROC of the MLAs for the binary detection problem. (a) Performance evaluation on the simulated dataset. (b) Performance evaluation on the Lynx dataset.

Finally, when analyzing the feature usage in the construction of the RFC, Fig. 6, it can be noted that the information contained in the peaks of the DFrFT plane are the most relevant features for classifying IF curves of slow-time history data (features #36-53). The central part of the histogram also contributes with useful features (features #10-20, the histogram range from feature #1 to #32) and, among the statistics contained in the feature vector, only the energy of the signal, which is also the variance for zero-mean signals, contributes with useful information (feature #35).
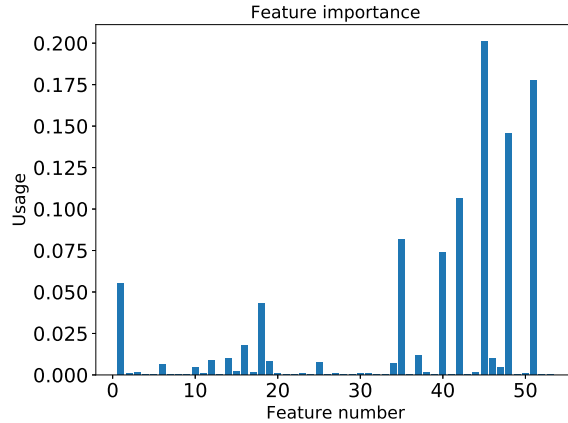

Figure 6: Feature usage of the constructed Random Forest classifier for binary classification problem. The features #1-32 correspond to histogram values. The features #33-35 are statistics. The features #36-53 are the relative magnitude, frequency index and chirp rate index of the 6 highest peaks in the DFrFT plane. The feature were obtained from the IF of the SAR signal following the procedure described in Alg. 1

7. CONCLUSIONS

In this paper, two different schemes for the detection of vibrating objects in SAR images have been developed and tested. The first detection scheme is a model-based data-driven approach that utilizes features extracted with the help of the DFRFT to feed a machine-learning classifier. The second detection scheme is purely model-based and uses a probabilistic model of the SAR slow-time signal, the KLT, and a likelihood-ratio detector. The results show that, after testing the two detection schemes with both simulated and real SAR data, the two detection schemes can be used to achieve high-performance vibrating-object detectors. These results are key because, one the one hand, they validate our models and the fact that it is feasible to train a machine-learning algorithm with simulated data generated via proper modeling and, on the other hand, they show that the IF of

the SAR SoI is a sufficient statistic for the detection of vibrating objects. Among the two implemented detectors we noticed that the data-driven one achieves a higher performance when there are no outliers. However, in the opposite case, the probabilistic detector is much more robust. Since surface vibrations are intrinsically linked to the vibrating source that generates them, the proposed techniques may enable one to detect and characterize concealed vibrating objects.

In the future, this work will be extended for performing m-ary detection (i.e., classification) of vibrational signatures retrieved from SAR images considering not only stationary sinusoidal waveforms, but also non-stationary vibrational signals such as chirped sinusoids. Also, the performance of the proposed detectors will be studied in the presence of clutter and noise at different intensity levels. In addition, we will incorporate the Hankel rank reduction (HRR) method[5, 21–23] to remove clutter from the data as a pre-processing step.

APPENDIX A. EXPRESSIONS FOR THE COVARIANCE MATRIX OF THE SIGNAL OF INTEREST

For this purpose, recall that the hypothesis testing problem can be written in vector form as in (6). Under hypothesis H_0 the slow-time vector $\mathbf{S} = \mathbf{S}_0 + \mathbf{W}$. Thus, the mean value (expected value) of $\mathbf{S}$ is given by

$$
\begin{aligned}
E\{\mathbf{S}\} &= E\big\{\big[S[0],\ldots,S[N-1]\big]^T\big\} = \big[E\{S[0]\},\ldots,E\{S[N-1]\}\big]^T \\
&= \big[E\{S_0[0]\},\ldots,E\{S_0[N-1]\}\big]^T,
\end{aligned}
\tag{12}
$$

where

$$
E\{S_0[n]\} = \int_{\Sigma,\Phi,Y} \sigma \exp\big(jf_y n + j\phi\big) f_{\Sigma,\Phi,Y}(\sigma,\phi,y)d(\sigma,\phi,y), \quad 0 \leq n \leq N-1.
\tag{13}
$$

Since Σ, Φ and Y are independent random variables with uniform distributions, then

$$
E\{S_0[n]\} = \frac{1}{\sigma_{max}-\sigma_{min}}\frac{1}{2y_o}\frac{1}{2\pi}\int_{-y_o}^{y_o}\int_{\sigma_{min}}^{\sigma_{max}}\int_{-\pi}^{\pi} \sigma \exp\big(jf_y n + j\phi\big)d\phi d\sigma d_y.
\tag{14}
$$

Note that the integral is zero because

$$
\int_{-\pi}^{\pi} \sigma \exp\big(jf_y n + j\phi\big)d\phi = 0,
\tag{15}
$$

then, $E\{S_0[n]\} = 0, \quad 0 \leq n \leq N-1$, and therefore

$$
E\{\mathbf{S}\} = \mathbf{0}_{N\times 1}.
\tag{16}
$$

Since $\mathbf{S}$ is zero-mean, the auto-covariance of $\mathbf{S}$ is given by

$$
\mathbf{cov}\{\mathbf{S}\} = E\{\mathbf{S}\mathbf{S}^*\},
\tag{17}
$$

where the symbol "$*$" represents the conjugate transpose.

$$
\begin{aligned}
\mathbf{cov}\{\mathbf{S}\} &= E\{(\mathbf{S}_0+\mathbf{W})(\mathbf{S}_0+\mathbf{W})^*\}, \\
&= E\{\mathbf{S}_0\mathbf{S}_0^*\} + E\{\mathbf{S}_0\mathbf{W}^*\} + E\{\mathbf{W}\mathbf{S}_0^*\} + E\{\mathbf{W}\mathbf{W}^*\}, \\
&= E\{\mathbf{S}_0\mathbf{S}_0^*\} + E\{\mathbf{W}\mathbf{W}^*\},
\end{aligned}
\tag{18}
$$

because $E\{\mathbf{W}\} = \mathbf{0}_{N\times 1}$, and $\mathbf{S}_0$ and $\mathbf{W}$ are independent. The value for the entry in the n-th position of the diagonal of the covariance matrix $\mathbf{cov}\{\mathbf{S}\}$ is given by

$$
\mathbf{cov}\{S[n],S[n]\} = E\{S_0[n]S_0^*[n]\} + E\{W[n]W^*[n]\} = E\{|\,S_0[n]\,|^2\} + E\{|\,W[n]\,|^2\},
\tag{19}
$$

where $E\{|\,W[n]\,|^2\} = \sigma_w^2$ and

$$
\begin{aligned}
E\{|\,S_0[n]\,|^2\} &= E\{|\,\Sigma\exp\left(jf_yYn+j\Phi\right)\,|^2\} = E\{|\,\Sigma\,|^2|\exp\left(jf_yYn+j\Phi\right)\,|^2\} \\
&= E\{|\,\Sigma\,|^2\}
\end{aligned}
\tag{20}
$$

$$
\begin{aligned}
E\{|\,\Sigma\,|^2\} &= \frac{1}{\sigma_{max}-\sigma_{min}}\int_{\sigma_{min}}^{\sigma_{max}}\sigma^2 d\sigma \\
&= \tfrac{1}{3}\left(\sigma_{max}^2 + \sigma_{max}\sigma_{min} + \sigma_{min}^2\right) \\
&=: \tfrac{1}{3}k_\sigma
\end{aligned}
\tag{21}
$$

Hence, $\mathbf{cov}\{S[n], S[n]\} = \tfrac{1}{3}k_\sigma + \sigma_w^2$. The value for off-diagonal entries of $\mathbf{cov}\{\mathbf{S}\}$ are given by

$$
\mathbf{cov}\{S[n], S[k]\} = E\{S_0[n]S_0^*[k]\} + E\{W[n]W^*[k]\} = E\{S_0[n]S_0^*[k]\},
\tag{22}
$$

because the clutter-noise samples are independent.

$$
\begin{aligned}
\mathbf{cov}\{S[n], S[k]\} &= E\{S_0[n]S_0^*[k]\} \\
&= E\{\left(\Sigma\exp\left(jf_yYn+j\Phi\right)\right)\left(\Sigma\exp\left(jf_yYk+j\Phi\right)\right)^*\} \\
&= E\{|\,\Sigma\,|^2\}E\{\exp\left(jf_yY(n-k)\right)\},
\end{aligned}
\tag{23}
$$

because the random variables Σ, Φ and Y are independent. Since

$$
E\{\exp\left(jf_yY(n-k)\right)\} = \frac{1}{2y_o}\int_{-y_o}^{y_o}\exp\left(jf_yy(n-k)\right)dy = \frac{\sin(y_of_y(n-k))}{y_of_y(n-k)},
\tag{24}
$$

then

$$
\mathbf{cov}\{S[n], S[k]\} = \frac{1}{3}k_\sigma\operatorname{sinc}(y_of_y(n-k)), \quad \forall n \neq k.
\tag{25}
$$

Finally, the (n, k)th entry of the $N \times N$ covariance matrix of $\mathbf{S}$ under H_0 is

$$
\mathbf{cov}\{S[n], S[k]\} = \begin{cases} \tfrac{1}{3}k_\sigma + \sigma_w^2, & 0 \leq n = k \leq N-1 \\ \tfrac{1}{3}k_\sigma\operatorname{sinc}(y_of_y(n-k)), & \forall n \neq k. \end{cases}
\tag{26}
$$

Under hypothesis H_1 the slow-time vector $\mathbf{S} = \mathbf{S}_1 + \mathbf{W}$. Proceeding in the same fashion as before, it is possible to obtain that

$$
E\{S_1[n]\} = 0, \quad 0 \leq n \leq N-1.
\tag{27}
$$

Therefore,

$$
E\{\mathbf{S}\} = \mathbf{0}_{N\times 1}.
\tag{28}
$$

Then, because $\mathbf{S}$ is zero-mean, the covariance matrix of $\mathbf{S}$ under H_1 is given by

$$
\begin{aligned}
\mathbf{cov}\{\mathbf{S}\} &= E\{\mathbf{S}\mathbf{S}^*\} \\
&= E\{(\mathbf{S}_1 + \mathbf{W})(\mathbf{S}_1 + \mathbf{W})^*\} \\
&= E\{\mathbf{S}_1\mathbf{S}_1^*\} + E\{\mathbf{S}_1\mathbf{W}^*\} + E\{\mathbf{W}\mathbf{S}_1^*\} + E\{\mathbf{W}\mathbf{W}^*\} \\
&= E\{\mathbf{S}_1\mathbf{S}_1^*\} + E\{\mathbf{W}\mathbf{W}^*\},
\end{aligned}
\tag{29}
$$

because $E\{\mathbf{W}\} = \mathbf{0}_{N\times 1}$ and $\mathbf{W}$ and $\mathbf{S}_1$ are independent. The value for the entry in the n-th position of the diagonal of $\mathbf{cov}\{\mathbf{S}\}$ is given by

$$
\begin{aligned}
\mathbf{cov}\{S[n], S[n]\} &= E\{S_1[n]S_1^*[n]\} + E\{W[n]W^*[n]\} \\
&= E\{|\,S_1[n]\,|^2\} + E\{|\,W[n]\,|^2\},
\end{aligned}
\tag{30}
$$

where $E\{| W[n] |^2\} = \sigma_w^2$ and

$$
\begin{aligned}
E\{| S_1[n] |^2\} &= E\{| \Sigma \exp\left(jf_yYn + j\Phi + jA\cos(\Phi_x + 2\pi nF)\right) |^2\} \\
&= E\{| \Sigma |^2| \exp\left(jf_yYn + j\Phi + jA\cos(\Phi_x + 2\pi nF)\right) |^2\} \\
&= E\{| \Sigma |^2\} \\
&= \tfrac{1}{3}k_\sigma.
\end{aligned}
\tag{31}
$$

Hence, $\mathbf{cov}\{S[n], S[n]\} = \tfrac{1}{3}k_\sigma + \sigma_w^2$. The value for off-diagonal entries of $\mathbf{cov}\{\mathbf{S}\}$ are given by

$$
\mathbf{cov}\{S[n], S[k]\} = E\{S_1[n]S_1^*[k]\} + E\{W[n]W^*[k]\} = E\{S_1[n]S_1^*[k]\},
\tag{32}
$$

because the clutter-noise samples are independent.

$$
\begin{aligned}
&\mathbf{cov}\{S[n], S[k]\} = E\{S_1[n]S_1^*[k]\} \\
&= E\{\left(\Sigma \exp\left(jf_yYn + j\Phi + jA\cos(\Phi_x + 2\pi nF)\right)\right) \\
&\quad\left(\Sigma \exp\left(jf_yYk + j\Phi + jA\cos(\Phi_x + 2\pi kF)\right)\right)^*\} \\
&= E\{| \Sigma |^2\} \cdot E\{\exp\left(jf_yY(n-k)\right)\} \cdot \\
&\quad E\{\exp\left(jA(\cos(\Phi_x + 2\pi nF) - \cos(\Phi_x + 2\pi kF))\right)\},
\end{aligned}
\tag{33}
$$

because all the involved random variables are independent. The expected value $g_{A,F,\Phi_x} = E\{\exp\left(jA(\cos(\Phi_x + 2\pi nF) - \cos(\Phi_x + 2\pi kF))\right)\}$ does not have a closed-form solution and it has to be carried out by numerical integration. Since

$$
E\{| \Sigma |^2\}E\{\exp\left(jf_yY(n-k)\right)\} = \frac{1}{3}k_\sigma \mathrm{sinc}(y_o f_y(n-k)), \quad \forall n \neq k,
\tag{34}
$$

the (n, k)th entry of the $N \times N$ covariance matrix of $\mathbf{S}$ under H_1 is given by

$$
\mathbf{cov}\{S[n], S[k]\} = \begin{cases} \frac{1}{3}k_\sigma + \sigma_w^2, & 0 \leq n = k \leq N-1 \\ \frac{1}{3}k_\sigma \mathrm{sinc}(y_o f_y(n-k))g_{A,F,\Phi_x}, & \forall n \neq k. \end{cases}
\tag{35}
$$

Note:
(1) Both resulting covariance matrices under hypothesis H_0 (26) and H_1 (35) are real-valued.
(2) A similar procedure can be followed to show that the pseudo-covariance matrix of $\mathbf{S}$ under both hypothesis, H_0 and H_1, is zero, i.e., $E_{H_j}\{\mathbf{S}\mathbf{S}^T\} = \mathbf{0}_{N \times N}$, $j = 0, 1$.

APPENDIX B. KARHUNEN-LOÈVE EXPANSION OF THE SIGNAL OF INTEREST

The KL expansion, also known as KLT in finite dimensional spaces, provides a mechanism for converting a discrete-time random process (i.e., random vector) into an equivalent sequence with diagonal autocovariance matrix. This is, the samples of the equivalent sequence are statistically independent among them. Specifically, the KL expansion of a random vector is carried out by projecting it onto the eigenvectors of its autocovariance matrix. Given a zero-mean random vector $\mathbf{S} = \left[S[0], \ldots, S[N-1]\right]^T$, with $N \times N$ autocovariance matrix $\mathbf{cov}\{\mathbf{S}\}$, the spectral decomposition of its autocovariance matrix is given by

$$
\mathbf{cov}\{\mathbf{S}\} = \sum_{k=0}^{N-1} \lambda_k \mathbf{v}_k \mathbf{v}_k^*,
\tag{36}
$$

where $\{\lambda_k\}_{k=0}^{N-1}$ and $\{\mathbf{v}_k\}_{k=0}^{N-1}$ are the eigenvalues and the orthonormal eigenvectors of $\mathbf{cov}\{\mathbf{S}\}$, respectively. The KL expansion of $\mathbf{S}$ [9, pp. 274-277] is defined as

$$
\mathbf{S} = \sum_{k=0}^{N-1} Z_k \mathbf{v}_k,
\tag{37}
$$

where the KL coefficients are

$$Z_k = \mathbf{v}_k^* \mathbf{S}, \quad 0 \le k \le N - 1. \tag{38}$$

The KL expansion separates the randomness and the time-variation characteristic of the discrete-time random process $\mathbf{S} = \begin{bmatrix} S[0], \ldots, S[N-1] \end{bmatrix}^T$. In particular, the randomness in $\mathbf{S}$ is summarized in the sequence $\mathbf{Z} = \{Z_k\}_{k=0}^{N-1}$ while the time variation in the process is captured in the sequence of eigenvectors $\{\mathbf{v}_k\}_{k=0}^{N-1}$. In this way, the expansion (37) combines these two properties to represent the process. Since $\{Z_k\}_{k=0}^{N-1}$ is determined from $\mathbf{S}$ via (38) and $\mathbf{S}$ is determined from $\{Z_k\}_{k=0}^{N-1}$ via (37), the sequence $\mathbf{Z}$ is an equivalent observation of the discrete-time process $\mathbf{S}$. Also, note that

$$E\{Z_k\} = E\{\mathbf{v}_k^* \mathbf{S}\} = \mathbf{v}_k^* E\{\mathbf{S}\} = 0, \tag{39}$$

and

$$\begin{aligned} \mathbf{cov}\{Z_k, Z_m\} &= E\{Z_k Z_m^*\} = E\{\mathbf{v}_k^* \mathbf{S} \times \left(\mathbf{v}_m^* \mathbf{S}\right)^*\} \\ \mathbf{cov}\{Z_k, Z_m\} &= E\{\mathbf{v}_k^* \mathbf{S} \mathbf{S}^* \mathbf{v}_m\} = \mathbf{v}_k^* \mathbf{cov}\{\mathbf{S}\} \mathbf{v}_m. \end{aligned} \tag{40}$$

Since $\mathbf{v}_k^* \mathbf{v}_m = \delta_{k,m}$ where $\delta_{k,m}$ is the Kronecker delta function and $\mathbf{cov}\{\mathbf{S}\}$ is given by (36), then

$$\mathbf{cov}\{Z_k, Z_m\} = \begin{cases} \lambda_k, & k = m \\ 0, & k \ne m. \end{cases} \tag{41}$$

Hence, $\mathbf{cov}\{\mathbf{Z}\} = \mathrm{diag}\left(\{\lambda_k\}_{k=0}^{N-1}\right)$. Finally, since under both hypotheses H_0 and H_1 the covariance matrices are real, then eigenvectors $\{\mathbf{v}_k\}_{k=0}^{N-1}$ are real.

ACKNOWLEDGMENTS

REFERENCES

[1] Wang, Q., Pepin, M., Beach, R. J., Dunkel, R., Atwood, T., Santhanam, B., Gerstle, W., Doerry, A. W., and Hayat, M. M., "Sar-based vibration estimation using the discrete fractional fourier transform," *IEEE Transactions on Geoscience and Remote Sensing* **50**, 4145–4156 (Oct 2012).

[2] Campbell, J. B., Pérez, F., Wang, Q., Santhanam, B., Dunkel, R., Doerry, A. W., Atwood, T., and Hayat, M. M., "Remote vibration estimation using displaced-phase-center antenna sar for strong clutter environments," *IEEE Transactions on Geoscience and Remote Sensing* **56**, 2735–2747 (May 2018).

[3] Wang, Q., Pepin, M., Dunkel, R., Atwood, T., Doerry, A. W., Santhanam, B., Gerstle, W., and Hayat, M. M., "Reduction of vibration-induced artifacts in synthetic-aperture-radar imagery using the fractional fourier transform," in [*2012 19th IEEE International Conference on Image Processing*], 2677–2680 (Sept 2012).

[4] Pérez, F., Campbell, J. B., Jaramillo, M., Dunkel, R., Atwood, T., Doerry, A., Gerstle, W. H., Santhanam, B., and Hayat, M. M., "Exploiting synthetic aperture radar imagery for retrieving vibration signatures of concealed machinery," in [*Proc.SPIE*], **9829**, 9829 – 9829 – 12 (2016).

[5] Pérez, F., Santhanam, B., Dunkel, R., and Hayat, M. M., "Clutter suppression via hankel rank reduction for dfrft-based vibrometry applied to sar," *IEEE Geoscience and Remote Sensing Letters* **14**, 2052–2056 (Nov 2017).

[6] Raney, R. K., "Synthetic aperture imaging radar and moving targets," *IEEE trans. on Aerospace and Electronic Systems* **7**(3), 499–505 (May 1971).

[7] Subotic, N. S., Thelen, B. J., and Carrara, D. A., "Cyclostationary signal models for the detection and characterization of vibrating objects in sar data," in [*Conference Record of Thirty-Second Asilomar Conference on Signals, Systems and Computers (Cat. No.98CH36284)*], **2**, 1304–1308 vol.2 (Nov 1998).

[8] Vargas-Rubio, J. G. and Santhanam, B., "On the multiangle centered discrete fractional fourier transform," *IEEE Signal Processing Letters* **12**, 273–276 (April 2005).

 [9] Poor, H. V., [*An introduction to signal detection and estimation*], Springer Science & Business Media (2013).

[10] Jakowatz, C. V., Wahl, D. E., Eichel, P. H., Ghiglia, D. C., and Thompson, P. A., [*Spotlight-mode Synthetic Aperture Radar: A Signal Processing Approach*], Springer Science+Business Media, New York, NY (1996).

[11] Wang, Q., Pepin, M., Santhanam, B., Atwood, T., and Hayat, M. M., "Sar-based vibration retrieval using the fractional fourier transform in slow time," in [*Radar Sensor Technology XIV*], Ranney, K. I. and Doerry, A. W., eds., *Proc. SPIE* **7669** (2010). doi: 10.1117/12.849671.

[12] Rüegg, M., Meier, E., and Nüesch, D., "Vibration and rotation in millimeter-wave sar," *IEEE trans. Geoscience and Remote Sensing* **45**(2) (Feb. 2007).

[13] Chen, V. C., Li, F., Ho, S. S., and Wechsler, H., "Micro-doppler effect in radar: phenomenon, model, and simulation study," *IEEE Transactions on Aerospace and Electronic Systems* **42**, 2–21 (Jan 2006).

[14] Soumekh, M., [*Synthetic Aperture Radar Signal Processing with MATLAB Algorithms*], Wiley, New York (1999).

[15] Flandrin, P., [*Time-Frequency/Time-Scale Analysis.*], no. v. 10 in Wavelet Analysis and Its Applications, Academic Press (1999).

[16] Namias, V., "The fractional order fourier transform and its applications to quantum mechanics," *J. Inst. Math Appl.* **25**, 241–265 (1980).

[17] Santhanam, B. and McClellan, J. H., "The discrete rotational fourier transform," *IEEE Trans. Signal Processing* **44**(4), 994–998 (1996).

[18] Vargas-Rubio, J. G. and Santhanam, B., "On the multiangle centered discrete fractional fourier transform," *IEEE Signal Processing Letters* **12**, 273–276 (2005).

[19] Gron, A., [*Hands-On Machine Learning with Scikit-Learn and TensorFlow: Concepts, Tools, and Techniques to Build Intelligent Systems*], O'Reilly Media, Inc., 1st ed. (2017).

[20] Abadi, M., Agarwal, A., Barham, P., Brevdo, E., Chen, Z., Citro, C., Corrado, G. S., Davis, A., Dean, J., Devin, M., Ghemawat, S., Goodfellow, I., Harp, A., Irving, G., Isard, M., Jia, Y., Jozefowicz, R., Kaiser, L., Kudlur, M., Levenberg, J., Mané, D., Monga, R., Moore, S., Murray, D., Olah, C., Schuster, M., Shlens, J., Steiner, B., Sutskever, I., Talwar, K., Tucker, P., Vanhoucke, V., Vasudevan, V., Viégas, F., Vinyals, O., Warden, P., Wattenberg, M., Wicke, M., Yu, Y., and Zheng, X., "TensorFlow: Large-scale machine learning on heterogeneous systems," (2015). Software available from tensorflow.org.

[21] DiMonte, C. L. and Arun, K. S., "Tracking the frequencies of superimposed time-varying harmonics," in [*International Conference on Acoustics, Speech, and Signal Processing*], 2539–2542 vol.5 (Apr 1990).

[22] Poon, M. W. Y., "A clutter suppression scheme for high frequenccy (hf) radar," *Master's thesis* (Faculty of Engineering and Applied Science, Memorial University of Newfoundland, Newfoundland and Labrador, Canada, 1991).

[23] Poon, M. W. Y., Khan, R. H., and Le-Ngoc, S., "A singular value decomposition (svd) based method for suppressing ocean clutter in high frequency radar," *IEEE Transactions on Signal Processing* **41**, 1421–1425 (Mar 1993).